Plasma Sources Sci. Technol. 3 (1994) 49–57. Printed in the UK

Helicon waves in a non-uniform plasma

Francis F Chen†‡§, M Johannes Hsieh§ and Max Light†

†Electrical Engineering Department, University of California, Los Angeles, CA 90024–1594, USA
‡Institute of Plasma and Fusion Research, University of California, Los Angeles, CA 90024–1597, USA
§ Engineering Research Center for Plasma-Aided Manufacturing, University of Wisconsin, Madison, WI 53706–1608, USA

Received 26 May 1993, in final form 17 August 1993

Abstract. The dispersion relation for helicon waves in a cold plasma of radially varying density has been reduced to compact form, and the radial eigenmodes have been computed for different density profiles. The results show a marked asymmetry between the left- and right-hand circularly polarized modes: the $m = -1$ (left) mode has a centrally peaked wave intensity and resonates with a much higher central density than the $m = +1$ mode. Positive feedback is therefore possible, leading to nonlinear channelling of the discharge. At a radius where the density falls to a certain value, a singularity arises in the coefficients of the wave equation; care must be taken in integrating through this point. This singularity has no physical significance. The marked difference between the $m = +1$ and -1 modes in a non-uniform plasma is caused by a difference in sign of the electron drift along the density gradient. Energy deposition is peaked near the radius of the peak in B_z, so that broad, uniform density profiles can be obtained by using the $m = +1$ mode and narrow, dense columns by using the $m = -1$ mode. These results explain many features observed by various groups over the past two years.

1. Introduction

Radio frequency (RF) discharges based on the excitation of helicon waves have been used for materials processing [1, 2] and laser applications [3]. The efficiency of absorption of RF power in helicon discharges has been explained by Chen [4] in terms of Landau damping acceleration of primary electrons. This hypothesis has been confirmed by the observation of electron tails in several experiments [5–7]. However, beginning with the ion cyclotron frequency experiments of Okamura *et al* [8], there has been poor agreement between theory and the density profiles produced by the various azimuthal modes $m = +1$, 0 and -1. Recent measurements of the change of profile with changes in magnetic field direction and antenna helicity [9–11] have revealed unexpected results: namely, the density profile changes dramatically from broad to narrow, depending on the sign of m or k.

Since the plasma density is never uniform in experiment, as it is in theory, we have reconsidered the helicon theory for non-uniform plasmas. Other workers (e.g. [12]) have done this previously, but the results were not clear, since the analytic treatment was not carried far enough before computation was begun. Our present results show a large asymmetry between the wave amplitude and energy deposition profiles of the $m = +1$ and -1 azimuthal modes, explaining the effects noted above. To match the vacuum region around the plasma, if any, we have incorporated the displacement current term throughout—no artificial boundary is assumed. We find a singularity in the equations which has not been noted before. This occurs when the density is sufficiently low that a helicon wave would be evanescent if the density were uniform. The singularity occurs well within the plasma for realistic profiles and would cause inconsistent results if not treated properly.

2. Dispersion equation

We consider the plasma in equilibrium to have an azimuthally symmetric density profile in a cylinder of radius a and a uniform axial magnetic field $B_0\hat{z}$. There are no zero-order electric fields or velocities; the diamagnetic drifts vanish by the assumption of zero temperature. The perturbations are of the form $\exp i(m\theta + kz - \omega t)$, so that $m = +1$ modes rotate clockwise when viewed along B_0, and $m = -1$ modes, counterclockwise. The governing equations are Maxwell's equations:

$$\nabla \cdot \boldsymbol{B} = 0 \tag{1}$$

$$\nabla \times \boldsymbol{E} = i\omega \boldsymbol{B} \tag{2}$$

$$\nabla \times \boldsymbol{B} = \mu_0(\boldsymbol{j} - i\omega\varepsilon_0 \boldsymbol{E}) \tag{3}$$

0963-0252/94/010049+09 $07.50

and the helicon assumption

$$j = -en_0(E \times B_0)/B_0^2. \tag{4}$$

Equation (4) states that the only plasma current is the $E \times B$ drift of the electrons; that is, the frequency is so high that the ions do not move, and is so low that the electron inertia and gyromotions can be neglected. We have also neglected all damping mechanisms. The subscript 1 has been suppressed on all first-order variables. The vector product of equation (4) with B_0 yields

$$j \times B_0 = (en_0/B_0^2)B_0 \times (E \times B_0) = en_0(E - E_z\hat{z}). \tag{5}$$

In the absence of plasma, a cylinder supports transverse electric (TE) and transverse magnetic (TM) modes, which are uncoupled. Since helicon waves in the absence of dissipation have $E_z = 0$ [4], we would expect them to couple to TE modes in the vacuum. Thus, we may take $E_z = 0$. Equation (5) then gives

$$E = (j \times B_0)/en_0. \tag{6}$$

Although this equation does not involve j_z, j_z does not vanish with E_z; it is given by equation (3). Using equation (6) in (3) we obtain

$$\begin{aligned} j &= \mu_0^{-1}\nabla \times B + i\omega\varepsilon_0 E \\ &= \mu_0^{-1}\nabla \times B + (i\omega\varepsilon_0/en_0)j \times B_0. \end{aligned} \tag{7}$$

We define

$$\alpha(r) \equiv \frac{\omega}{k}\frac{e\mu_0 n_0(r)}{B_0} \qquad k_0 \equiv \frac{\omega}{c} \tag{8}$$

so that equation (7) can be written

$$\mu_0 j = \nabla \times B + \frac{ik_0^2}{k\alpha}\mu_0 j \times \hat{z}. \tag{9}$$

We next use equation (6) for E in equation (2) to obtain

$$\begin{aligned} i\omega B &= \nabla \times \left(\frac{1}{en_0}(j \times B_0)\right) \\ &= B_0 \cdot \nabla\left(\frac{j}{en_0}\right) - B_0\nabla \cdot \left(\frac{j}{en_0}\right). \end{aligned} \tag{10}$$

Since n_0 does not vary with z, it needs to be differentiated only in the second term. The result is

$$i\omega B = \frac{B_0}{en_0}\left(ikj + \frac{n_0'}{n_0}j_r\hat{z} - \hat{z}\nabla \cdot j\right). \tag{11}$$

If B_0 is uniform, the definition of α in equation (8) implies that $\alpha'/\alpha = n_0'/n_0$. Equation (11) can then be written

$$\alpha B = \mu_0 j + \frac{i}{k}\mu_0\hat{z}\left(\nabla \cdot j - \frac{\alpha'}{\alpha}j_r\right). \tag{12}$$

Note that the perpendicular components obey the same relation as in a uniform plasma:

$$\mu_0 j = \alpha B_\perp \tag{13}$$

but the z component has two new terms. The $\nabla \cdot j$ term arises from the displacement current, as seen from the divergence of equation (3), and the α' term from the density gradient. Equation (9) then reduces to

$$\mu_0 j = \nabla \times B + \frac{i}{k}k_0^2 B \times \hat{z}. \tag{14}$$

To evaluate $\nabla \cdot j$, take the divergence of equation (14):

$$\mu_0\nabla \cdot j = \frac{i}{k}k_0^2\nabla \cdot (B \times \hat{z}) = \frac{i}{k}k_0^2(\nabla \times B)_z. \tag{15}$$

Finally, using equations (13)–(15) in (12), we obtain

$$\begin{aligned} \alpha B = (\nabla \times B)_\perp + \left(1 - \frac{k_0^2}{k^2}\right)(\nabla \times B)_z\hat{z} \\ + \frac{i}{k}(k_0^2 B \times \hat{z} - \alpha' B_r\hat{z}). \end{aligned} \tag{16}$$

We define

$$\gamma \equiv 1 - (k_0/k)^2 \tag{17}$$

and separate the r, 0, and z components of equation (16):

$$\alpha B_r = \frac{im}{r}B_z - ik\gamma B_\theta \tag{18}$$

$$\alpha B_\theta = -B_z' + ik\gamma B_r \tag{19}$$

$$\alpha B_z = \gamma\left(\frac{1}{r}(rB_\theta)' - \frac{im}{r}B_r\right) - \frac{i}{k}\alpha' B_r. \tag{20}$$

Eliminating B_θ and B_r from equations (18) and (19) respectively yields

$$\beta B_r = \frac{im}{r}\alpha B_z + ik\gamma B_z' \tag{21}$$

$$\beta B_\theta = -\alpha B_z' - \frac{m}{r}k\gamma B_z \tag{22}$$

where

$$\beta \equiv \alpha^2 - k^2\gamma^2. \tag{23}$$

Having expressed B_r and B_θ in terms of B_z we can now substitute equations (21) and (22) into (20) to obtain a differential equation for B_z. Finally, after some straightforward algebra and a few fortuitous cancellations, we obtain

$$B_z'' + f(r)B_z' + g(r)B_z = 0 \tag{24}$$

where

$$f(r) = \frac{1}{r} - \frac{2\alpha\alpha'}{\beta} \tag{25}$$

$$g(r) = \frac{\beta}{\gamma} - \frac{m^2}{r^2} - \frac{m}{k}\frac{\alpha'}{\gamma r}\left(1 + \frac{2k^2\gamma^2}{\beta}\right). \tag{26}$$

An equation similar to equation (24) has been considered by previous investigators [13–15], but its analysis leading to our conclusions has not been done before.

The displacement current can be neglected by setting $k_0 = 0$ in equation (17) so that $\gamma = 1$. In practice, $\gamma - 1$ is of order -10^{-4}, and is entirely negligible. Physically, this means that the coupling to radio waves outside the

plasma is weak because k is so much larger than k_0 that the free space waves are highly evanescent. The density gradient can be neglected by setting $\alpha' = 0$, in which case we recover the uniform plasma equations [4]. Once the eigenfunction $B_z(r)$ is known, the other components of $\boldsymbol{B}$ can be found from equations (21) and (22). The $\boldsymbol{E}$ field, given by equations (6) and (13), is perpendicular to $\boldsymbol{B}$ in each cross-sectional plane, and the relation is the same as for uniform plasmas [4]. However, the density gradient introduces a major difference in the terms proportional to α'/β in $f(r)$ and $g(r)$. In particular, the last term in $g(r)$ depends on the sign of m and is responsible for the changes in the observed appearance of helicon discharges when the helicity of the antenna is reversed. Note that the sign of k does not affect the α' terms, since α and α' also change sign with k. Thus, changing the direction of $\boldsymbol{B}$ relative to k should not affect the mode patterns.

The coefficients in equation (24) are singular at $\beta = 0$, or $\alpha^2 = k^2$ (for $\gamma = 1$). This is the radius where the density becomes too low to support a uniform helicon wave. That is, in a uniform plasma, the dispersion relation is

$$\alpha^2 = T^2 + k^2 \tag{27}$$

and when α^2 is less than k^2, the transverse wave number T becomes imaginary, and the wave changes to a surface wave. Since numerical integration is necessary anyway, the decomposition into body waves and surface waves is not meaningful. This singularity, which appears only when there is a density gradient, is only a mathematical problem and has no physical significance. In a non-uniform plasma, the wave fields vary smoothly over this point, but care must be taken to avoid numerical difficulties.

The boundary condition to be satisfied by the eigenfunctions of equation (24) is $j_r(a) = 0$ for an insulating tube of inside radius a. If the density is finite at the wall, equation (13) requires that B_r be zero there. Equation (6) gives $E_\theta = 0$, which is also the boundary condition for a conducting wall. If n_0, and hence α, vanishes at the wall, the helicon wave has to be matched, in principle, to the radiation field. However, in practice, the layer in which the displacement current dominates the conduction current is so thin that little error is engendered by taking $B_r(a) = 0$. Equation (24), then, is to be integrated subject to this and the condition that all fields be finite at $r = 0$.

3. Calculations

Density profiles with a peak on axis are modelled with a two-parameter family of curves:

$$\frac{n}{n_0} = \left[1 - \left(\frac{r}{a}\right)^s\right]^t \equiv p(r) \tag{28}$$

where $p(r)$ is the profile factor. Typical profiles for various pairs (s, t) are shown in figure 1.

Lengths are now scaled to the tube radius a, so that

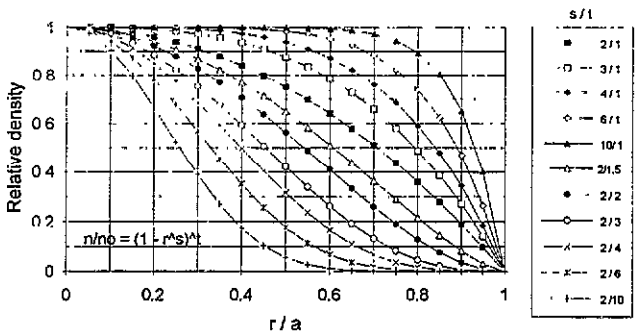

Figure 1. Density profiles represented by the parameters s and t.

$r \to r/a$, $k \to ka$, $\alpha \to \alpha a$, etc. Equations (24)–(26) retain the same form when the dimensionless quantities are used. Since $\alpha'/\alpha = p'/p$ when B_0 is constant, equations (24)–(26) can be written

$$B_z'' + f(r)B_z' + g(r)B_z = 0 \tag{29}$$

$$f(r) = \frac{1}{r} - \frac{p'}{p}\frac{2\alpha^2}{\beta} \tag{30}$$

$$g(r) = \frac{\beta}{\gamma} - \frac{m^2}{r^2} - \frac{m\alpha}{k\gamma r}\frac{p'}{p}\left(1 + \frac{2k^2\gamma^2}{\beta}\right) \tag{31}$$

where *all quantities are dimensionless.* Equation (29) is then integrated, starting at $r = 0$ with $B_z = 1$, $B_z' = 0$ for the $m = 0$ mode, and $B_z = 0$, $B_z' = 1$ for all other m numbers, and using the coefficients $f(r)$ and $g(r)$ given by equations (30) and (31). At each step B_r and B_θ are computed from equations (21) and (22). The values of k and k_0 (actually, ka and $k_0 a$) are fixed by assuming a wavelength and a frequency. In the curves given here, we have taken $f = 27.12$ MHz, $\lambda = 24$ cm and $a = 5$ cm. The eigenvalue α_0, representing αa at maximum density (on axis), is then varied until B_r vanishes at $r = 1$.

The singularity that occurs at $\beta = 0$ requires special treatment. If a grid point falls close to the radius where $\alpha^2(r) = k^2\gamma^2$, the coefficients $f(r)$ and $g(r)$ become extremely large. When this happens it is immediately obvious because the curves of $\boldsymbol{B}(r)$ are discontinuous there. Decreasing the grid spacing does not automatically avoid 'stepping on' the pole; that is, that the grid points fall asymmetrically around the singularity. We have used an adaptive step size scheme in which the integration starts with a step length $d_{\max}$, and d decreases in proportion to β down to a minimum value $d_{\min}$. Even so, it was sometimes necessary to adjust $d_{\max}$ or $d_{\min}$ to obtain smooth behaviour of $\boldsymbol{B}(r)$ through the singularity. From equations (21) and (22), it would appear that B_r and B_θ become infinite as β goes to zero. However, at this point B_z' is related to B_z by

$$B_z' = -(m/r)B_z \tag{32}$$

as can be verified by inserting the leading terms in equations (30) and (31) into equation (29). Then the right-hand sides of equations (21) and (22) also vanish precisely at the point where $\alpha = k\gamma$ and B_r and B_θ are

found to vary smoothly over the singular point. Sudit [16] has subsequently verified that the singularity is mathematical and not physical, by deriving and computing the equation for B_r. That equation has regular coefficients.

The difference in profiles of B_z among the $m = 0$, $m = +1$, and $m = -1$ modes is shown in figure 2 for a parabolic density profile ($s = 2, t = 1$). Since energy absorption roughly follows the profile of B_z, it is seen that broad discharges are best produced by the $m = +1$ mode. The frequency, wavelength and tube diameter are as given above, but the curves are almost universal because ω affects only the small displacement current correction, and k and r are scaled to the radius a. The absolute value of k is important only when one considers damping and antenna coupling. The position of the singularity is apparent in the curve of the $m = +1$ mode where the effect of adaptive step size appears as a change in the density of points.

Comparison of all three components of $\boldsymbol{B}$ for the $m = +1$ and -1 modes is shown in figure 3 for uniform plasmas and figure 4 for parabolic plasmas. The curves

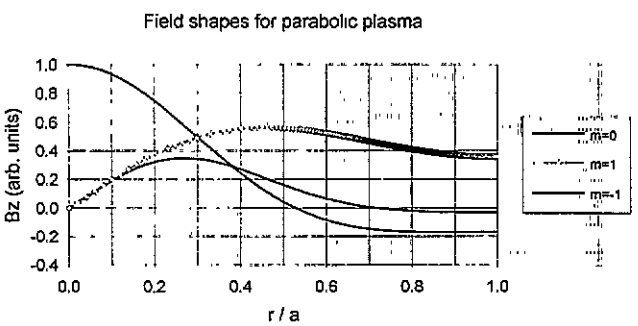

Figure 2. Radial profiles of B_z for the $m = 0, +1$, and -1 azimuthal modes for a parabolic density profile. The density of points for the $m = +1$ curve shows the effect of adaptive step size.

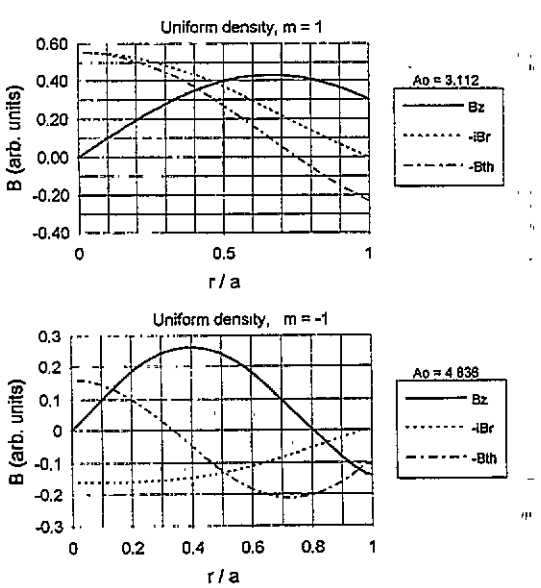

Figure 3. Comparison of $\boldsymbol{B}$ profiles for the $m = +1$ and -1 modes for a uniform plasma. The eigenvalue of α_0 is given as A_0.

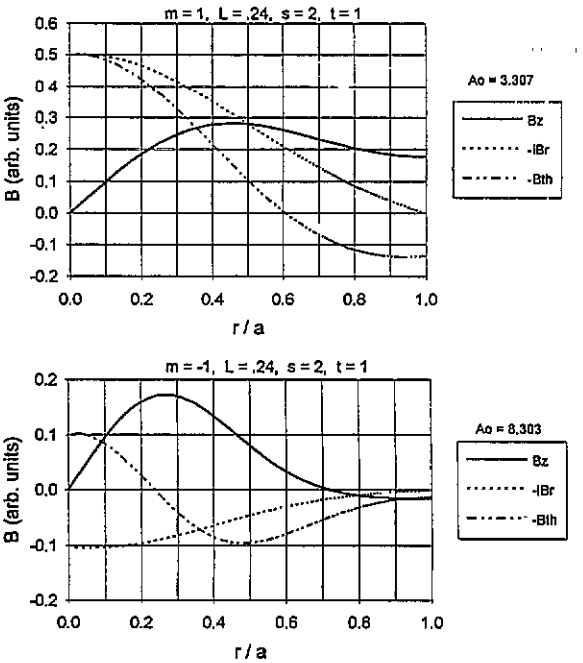

Figure 4. Comparison of profiles for the $m = +1$ and -1 modes for a parabolic density profile.

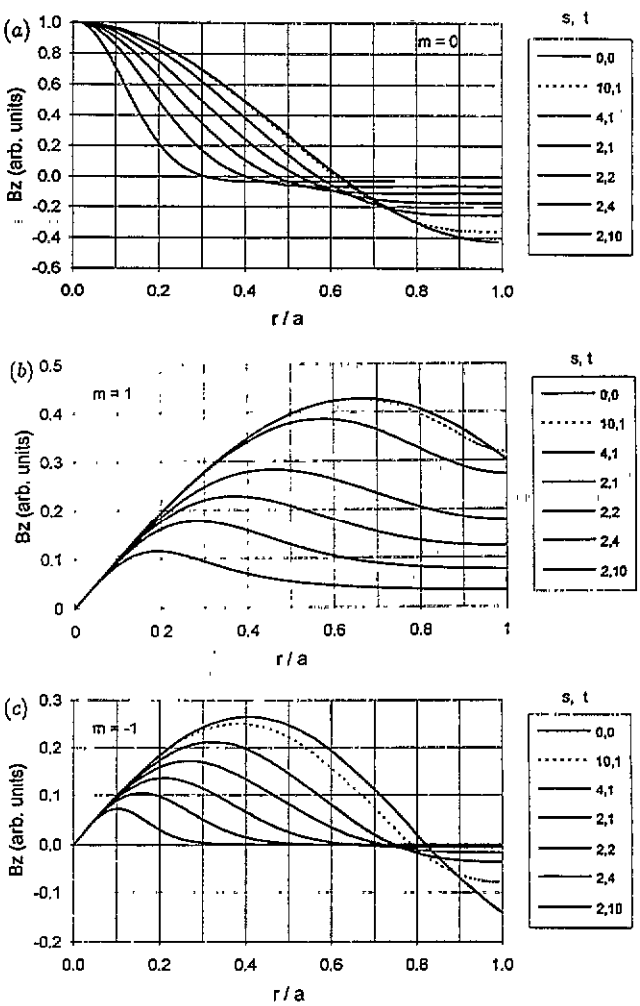

Figure 5. Behaviour of the radial profiles of B_z as the density profile is changed, for the (*a*) $m = 0$, (*b*) $m = +1$ and (*c*) $m = -1$ modes. The values (s, t) correspond to the density profiles shown in figure 1.

for uniform density were computed by the shooting technique and agree with the analytic solution in terms of Bessel functions [4]. The values of α_0 for each case are also given. The marked difference between the right- and left-handed helicons is evident even in the uniform case.

Figure 5 shows the B_z curves for various density profiles for the (*a*) $m = 0$, (*b*) $m = +1$, and (*c*) $m = -1$ modes. As expected, the wave profiles become steeper with the sharpness of the density profile. Figure 6 is an example of one of the other computed curves, in this case the B_θ component of the $m = -1$ mode, as the density profile is varied. The zero crossing point, which is easy to measure experimentally, progressively moves inward as the density profile sharpens. This point also separates the inner and outer regions of the B field patterns shown below.

The self-channelling effect of the $m = -1$ mode is clearly seen in figure 5(*c*): as the density steepens, the wave pattern is narrower, causing the ionization to occur ever closer to the axis. Figure 7 shows the profiles of all three components of $\boldsymbol{B}$ for the $m = -1$ mode for the narrowest density profile we have computed ($s = 2$, $t = 10$). These curves show what might be expected for the final, self-focused state for a diffusion limited, maximum density plasma column.

The value of α_0 for the lowest radial mode varies greatly with the azimuthal mode. Figure 8 shows the increase of α_0 with the parameter t in equation (28), as s is held constant at $s = 2$. As the discharge narrows, t increases and α_0 increases almost linearly with t for the $m = -1$ mode, while it remains nearly constant for the $m = +1$ mode. The $m = 0$ mode lies in between. At $t = 0$ (uniform plasma), α_0 for the $m = -1$ mode is only $\approx 50\%$ higher than for the $m = +1$ mode. At $t = 10$, however, α_0 for the $m = -1$ mode is almost an order of magnitude higher. Since, from equation (8), α_0 is proportional to the peak value of n_0/B_0, much higher peak densities can be expected from the $m = -1$ mode; or, conversely, for the same peak density, much lower B fields are needed. The positive feedback effect increases the value of t and further increases α_0. Each point in figure 8 was obtained by numerical integration for $\boldsymbol{B}$ as described above; the field profiles cannot all be given here.

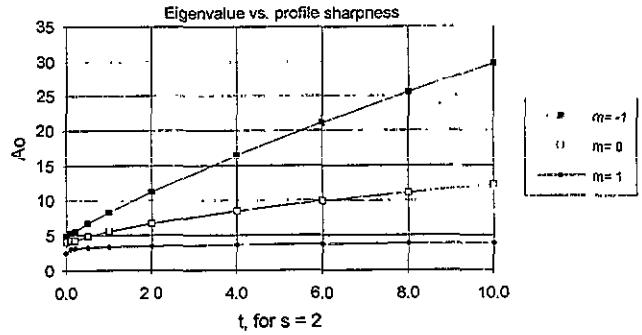

Figure 8. Variation of the eigenvalue α_0 with density peaking parameter t for the $m = -1$, 0, and $+1$ modes.

As k is increased keeping the tube radius constant, the effect of the k term in equation (27) becomes more important in determining the value of α. For a fixed frequency this corresponds to shortening the antenna and slowing down the wave velocity. Figure 9 shows the variation of α with wavelength $2\pi/k$ in a uniform plasma for the $m = +1$ and -1 modes, and figure 10 shows the corresponding change in the B_z profiles. The range of wavelengths computed in figures 9 and 10 corresponds to resonant electron energies of 30 eV to 7.7 keV.

We have also studied the eigenfunctions for higher order modes. Figure 11 shows, for instance, the second radial mode ($n = 2$) for $m = 0$ in a parabolic profile. The eigenvalue α_0 nearly doubles from 5.534 to 10.05, indica-

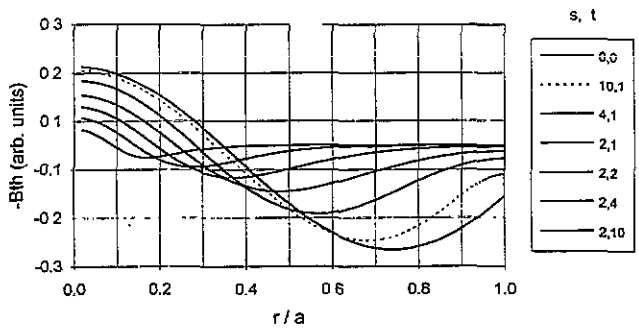

Figure 6. Behaviour of the radial profile of B_θ as the density profile is changed, for the $m = -1$ mode.

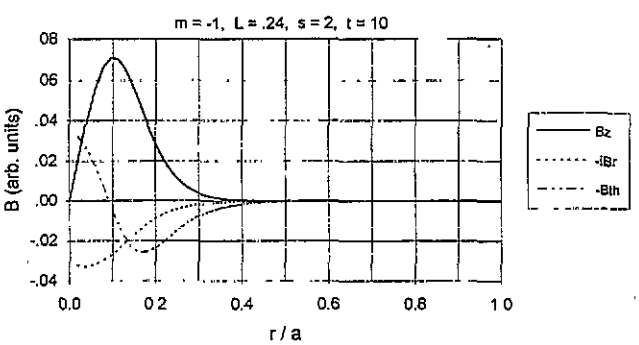

Figure 7. B field profiles for the $m = -1$ mode in a sharply peaked density profile.

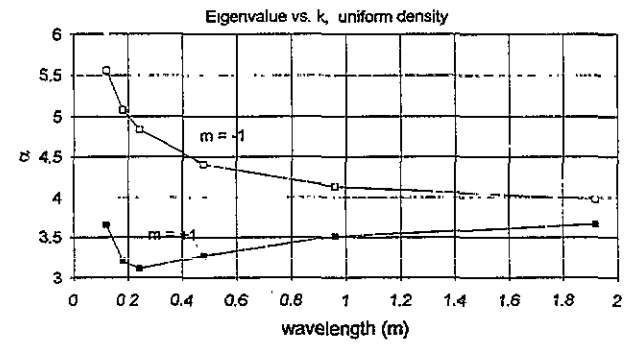

Figure 9. Variation of the eigenvalue α with parallel wavelength for the $m = +1$ and -1 modes in a uniform plasma. The tube radius was fixed at 5 cm.

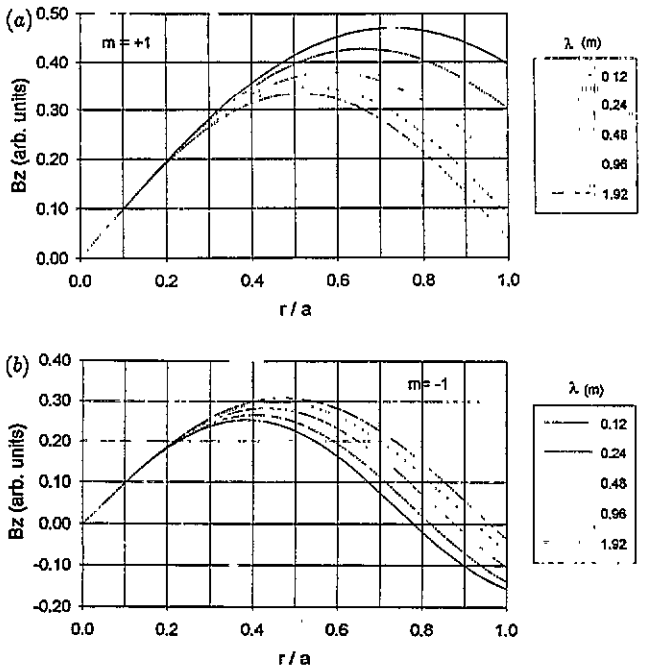

Figure 10. Variation of the B_z profile with wavelength for the (*a*) $m = +1$ and (*b*) $m = -1$ modes.

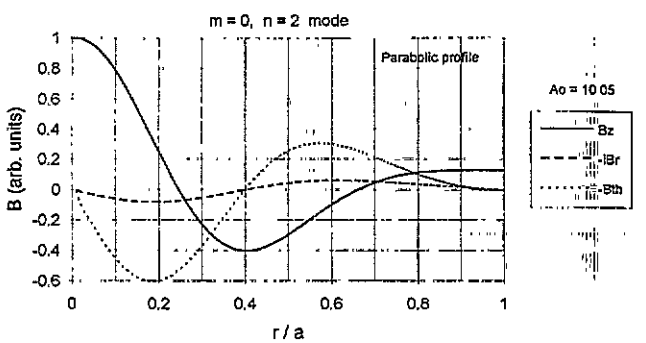

Figure 11. *B* field profiles for the second radial mode of $m = 0$ in a parabolic density profile.

ting a large increase in resonant peak density. Figure 12 shows this density increase for three azimuthal modes as the n number is increased. Figure 13 shows the field components for the $m = -2$ mode. In going from $m = -1$ to $m = -2$, the value of α_0 increases from 8.303 to 11.97, although the fields are peaked at a slightly larger radius.

Finally, the patterns for the electric and magnetic wave fields are shown in figures 14–16. In figures 14 and 15, the $m = +1$ and -1 mode patterns in a cross sectional plane, respectively, are compared for flat and parabolic density profiles. In figure 16, the *B* lines in the y–z plane are also shown. These projections indicate that individual *B* lines have all three components and therefore spiral in a complicated way.

4. Energy deposition and physical mechanism

Absorption of the RF energy occurs at the rate $E \cdot j$, which has only the term $E_z j_z$ because the current is

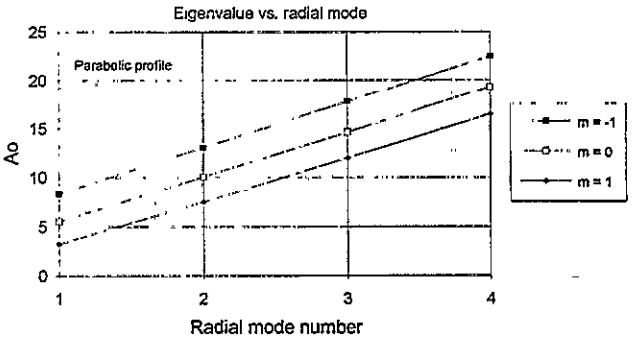

Figure 12. Variation of the eigenvalue α_0 with radial mode number for the $m = -1$, 0, and $+1$ modes.

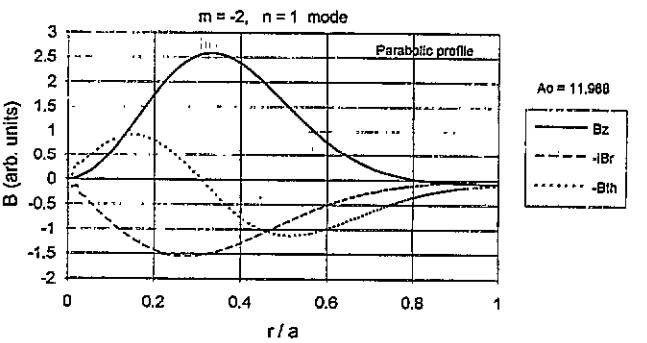

Figure 13. *B* field profiles for the second azimuthal mode in a parabolic profile.

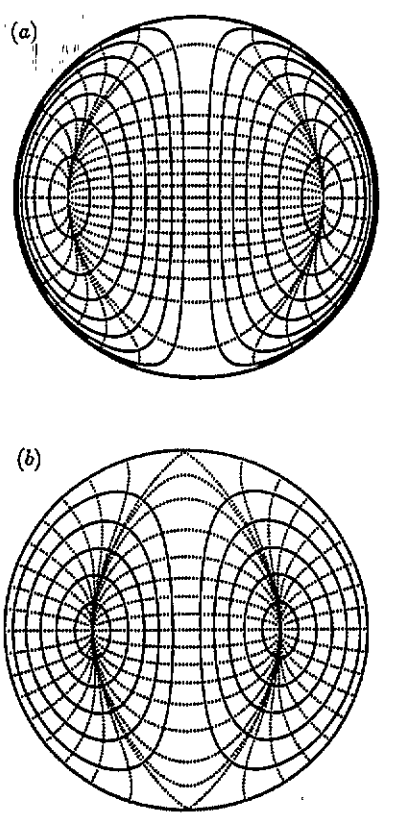

Figure 14. Field line patterns for the *B* field (full curves) and *E* field (dotted curves) in the x–y plane for the (*a*) $m = +1$ and (*b*) $m = -1$ modes in a uniform plasma.

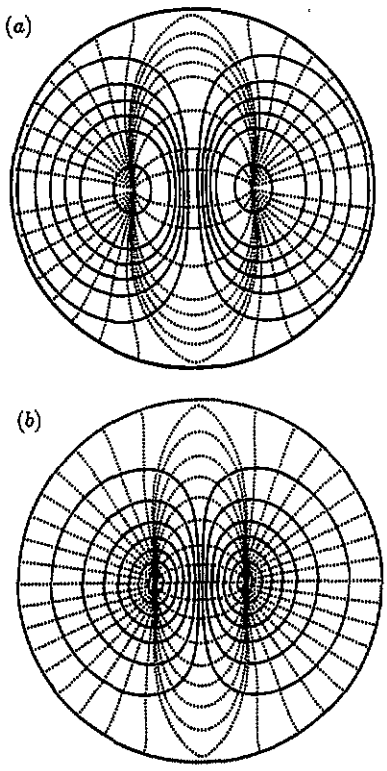

Figure 15. Field line patterns for the B field (full curves) and E field (dotted curves) in the $x-y$ plane for the (*a*) $m = +1$ and (*b*) $m = -1$ modes in a parabolic plasma.

perpendicular to E in the transverse plane. Although E_z vanishes in the undamped limit, it arises in the presence of damping in order to drive the current j_z. Without considering the details of the damping mechanism, we can say that the energy W absorbed per unit volume per second is approximately ηj_z^2, where η is an effective resistivity, and j_z is, for weak damping, given by the undamped solutions given here. The current j_z is given by equations (12) and (13):

$$\mu_0 j_z = \alpha B_z + \frac{i\mu_0}{k}\frac{\alpha'}{\alpha} j_r = \alpha\left(B_z + \frac{i}{k}\frac{\alpha'}{\alpha} B_r\right). \quad (33)$$

We have simplified this discussion by making the extremely good assumption that the $\nabla \cdot j$ (displacement current) term is negligible. If either Landau damping or electron–neutral collisions is dominant, η is proportional to $1/n_0$, and hence to $1/\alpha$. The absorption rate is then proportional to αj_z^2, or

$$W \propto |\alpha|\left(B_z + \frac{i}{k}\frac{\alpha'}{\alpha} B_r\right)^2. \quad (34)$$

The term containing α' in equations (33) and (34) represents the space charge that arises from current flow along the density gradient. This space charge has to be dispersed by current flow along z, since $\nabla \cdot j = 0$ in the absence of displacement current. Thus, the density inhomogeneity contributes a term which either increases or decreases j_z (and hence the absorption rate), depending on the sign of $iB_r\alpha'$ relative to that of B_z. This phase relation depends on the rotation direction of the mode, as can be seen from a modification of equation (21):

$$iB_r \simeq -\frac{m}{r}\frac{\alpha}{\beta} B_z. \quad (35)$$

Here we have neglected the B_z' term in equation (21) because most of the absorption occurs near the maximum of B_z and in a region where $\alpha^2 \gg k^2$. Substituting equation (35) into equation (34) gives

$$W \propto |\alpha| B_z^2\left(1 - \frac{m}{r}\frac{\alpha}{k}\frac{\alpha'}{\alpha}\frac{1}{\beta}\right)^2. \quad (36)$$

Since α' is negative, we see that the α' term increases W if $m > 0$, and decreases W if $m < 0$. Note that the sign of k does not matter since α contains k.

The radial variation of W is shown for the $m = +1$, -1 and 0 modes respectively, in figure 17(*a*)–(*c*). We see that the deposition profile generally follows that of B_z, but the magnitude of the absorption rate is affected differently by the density gradient term for the $m = +1$ and -1 modes, as explained above. This term has little or no effect on the $m = 0$ mode, as expected from equation (36). The location of the singularity in the computation is marked by the vertical line, which is a plot of $f(r)$, showing that the difference in the radii of maximum energy absorption is not related to the position of the singularity.

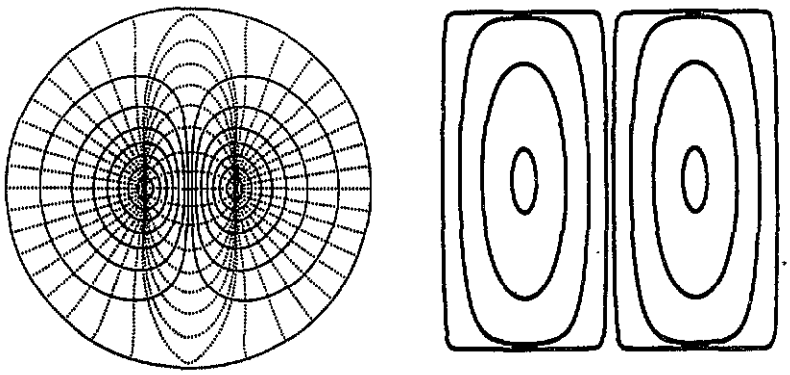

Figure 16. B field pattern for the $m = 1$ mode in the $y - x$ and $y - z$ planes for a parabolic plasma. The z scale (right diagram) has been shrunk.

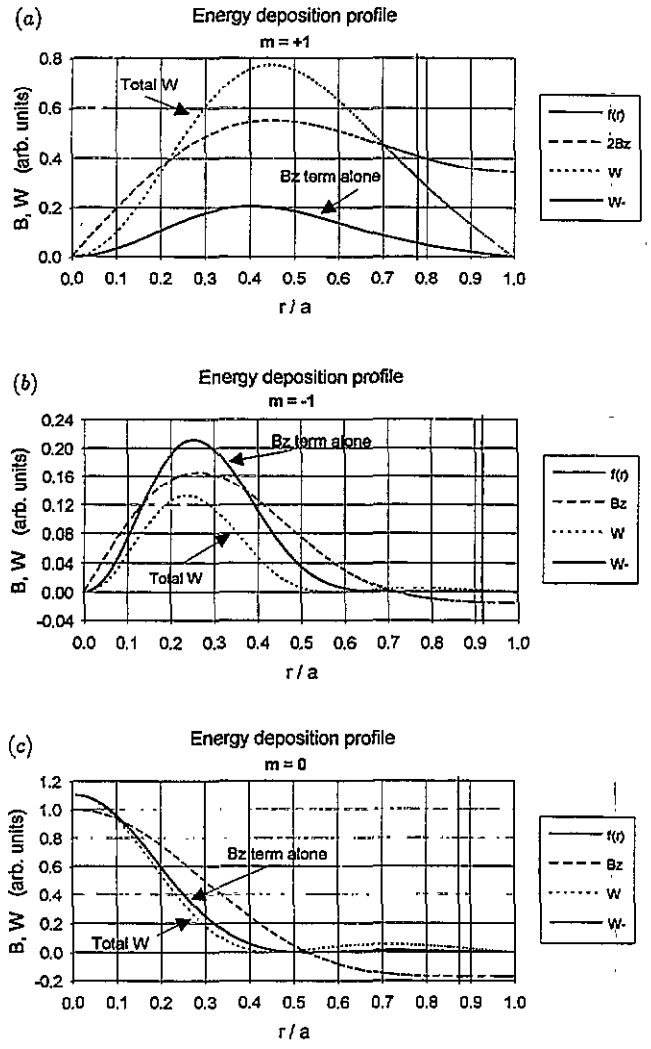

Figure 17. Energy deposition rate W against radius, as compared with the B_z profile, for the (*a*) $m = +1$, (*b*) $m = -1$ and (*c*) $m = 0$ modes in a parabolic plasma profile. The deposition profile without the density gradient effect is shown as W_-. The vertical line is a plot of $f(r)$, showing the location of the pole in this coefficient.

The reason for the difference in width of the $m = +1$ and $m = -1$ mode patterns is not as easily explained in terms of particle flows, but can be understood in mathematical terms. This difference is significant even for a uniform plasma. In figure 3, we see that at $r = 0$, B_θ and iB_r have the same magnitude but different sign for $m = +1$ and -1. This is because $\nabla \cdot \boldsymbol{B} = 0$, and the B_r/r and $(im/r)B_\theta$ terms in that relation dominate at small radii, while B_z goes to zero by symmetry. As the radius increases, B_r decreases smoothly to zero in both cases to satisfy the boundary condition at $r = a$. However, B_θ has to change sign to create the loops in the B field patterns of figures 14 and 15. At the boundary, since $j_r = (\nabla \times \boldsymbol{B})_r$ vanishes, the terms $(im/r)B_z$ and ikB_θ must be equal. Since B_z and B_θ started out with opposite sign at $r = 0$, and B_θ has changed sign, B_z does not change sign if $m > 0$, but changes sign if $m < 0$. Thus, the B_z profile has to be narrower for $m < 0$ than for $m > 0$. Since the energy absorption follows the curve of B_z, the left-hand polarized modes create more centrally peaked density profiles, which further narrows the B_z profile. Thus, left-hand helicons favour the production of dense, narrow columns, while right-hand helicons favour the production of broad, uniform discharges.

We note, however, that even right-hand helicons can undergo self-channelling into narrow columns if the left-hand helicon is not present. This was apparently observed by the Nagoya RFC-XX group [8] in an experiment on ion cyclotron resonance heating. There, the $m = +1$ mode produced a dense, narrow plasma, while the $m = -1$ mode produced a broad density profile, ostensibly in contradiction to our present conclusions. However, the Nagoya experiment had an additional heating mechanism (ICRH) which was operative with left-hand polarization, and hence the $m = -1$ helicon mode described here could not be observed. With right-hand polarization, ICRH could not occur, and the $m = +1$ helicon wave was responsible for the ionization. This gave rise to peaked profiles consistent with our computations for the $m = +1$ mode. It is just that the even narrower plasmas characteristic of the $m = -1$ helicon mode were masked by the ICRH effect. Note that for frequencies just below the ion cyclotron frequency, the radial current is still given by the electron $\boldsymbol{E} \times \boldsymbol{B}$ drift, as is the case in this paper, because the ion $\boldsymbol{E} \times \boldsymbol{B}$ drift is greatly reduced by the finite Larmor radius effect.

5. Design of helicon sources

The dimensionless graphs given in this paper can be used to optimize parameters for helicon plasma generators. We may set $k_0 = 0$, since the displacement current is negligible in any practical device. The first step is to fit the measured or conceptual density profile to the form of equation (28) to obtain the values of s and t for the best fit. For $s = 2$, the value of α_0 can be read from figure 8 for the most common azimuthal modes; for other values of s and m, plots like that of figure 8 would have to be calculated using the shooting procedure described here.

The dimensionless parameter α_0 is given by

$$\alpha_0 = \frac{\omega}{ka}\frac{n_0}{B_0} e\mu_0 a^2. \tag{37}$$

If the operating density is below about $10^{13}\,\mathrm{cm}^{-3}$ so that Landau damping is effective, it is best to decide first on the value of E_{eV}, the energy (in eV) of an electron moving at the phase velocity ω/k of the wave. In that case, equation (37) can be written as

$$\frac{n_{13}}{B_3} = 8.38\,\frac{\alpha_0}{a_{\mathrm{cm}}}\,E_{\mathrm{eV}}^{-1/2} \tag{38}$$

where n_{13} is the density in units of $10^{13}\,\mathrm{cm}^{-3}$, B_3 is the magnetic field in kG and a_{cm} is the tube radius in cm. To decide on the radius, an important consideration is the aspect ratio of the antenna, which, for good coupling, has to be not too long and not too short. A value

of 0.5–1 for ka is reasonable. Since ω/k is already fixed, this fixes a for given ω, or ω for given a. Equation (38) then gives the peak density which will support a helicon wave at any given magnetic field.

If the density is so high that particle resonances are not important, there is no constraint on ω/k. In that case, equation (37) can be written

$$\frac{n_{13}}{B_3} = 7.90\alpha_0 \frac{ka}{f_6 a_{\mathrm{cm}}^2} \tag{39}$$

where f_6^- is the frequency in MHz and α_0 is dimensionless.

Acknowledgments

This work was supported by the University of Wisconsin Engineering Research Center on Plasma-Aided Manufacturing under NSF Grant ECD-8721545, by the Lawrence Livermore National Laboratory Plasma Physics Research Institute under DOE Contract No. W-7405-ENG-48, and by the UCLA ATRI Program funded by AFOSR Contract No F30602-91-C-0020.

References

[1] Perry A J and Boswell R W 1989 *Appl. Phys. Lett.* **55** 148
[2] Kitagawa H, Tsunoda A, Shindo H and Horiike Y 1993 *Plasma Sources Sci. Technol.* **2** 11
[3] Zhu P and Boswell R W 1989 *Phys. Rev. Lett.* **63** 2805
[4] Chen F F 1991 *Plasma Phys. Control. Fusion* **33** 339
[5] Zhu P and Boswell R W 1991 *Phys. Fluids* B **3** 869
[6] Loewenhardt P K, Blackwell B D, Boswell R W, Conway G D and Hamberger S M 1991 *Phys. Rev. Lett.* **67** 2792
[7] Chen F F and Decker C D 1992 *Plasma Phys. Control. Fusion* **34** 635
[8] Okamura S *et al* 1986 *Nucl. Fusion* **26** 1491
[9] Shoji T and Sakawa Y 1992 Private communication
[10] Chen F F and Chevalier G 1992 *Int. Conf. Plasma Physics (Innsbruck, Austria) 1992* vol III (Innsbruck Institute for Ion Physics, University of Innsbruck) p 1701
[11] Chevalier G and Chen F F 1993 *J. Vac. Sci. Technol.* A **11** 1165
[12] Shoji T, Sakawa Y, Nakazawa S, Kadota K and Sato T 1993 *Plasma Sources Sci. Technol.* **2** 5
[13] Blevin H A and Christiansen P J 1966 *Australian J. Phys.* **19** 501
[14] Davies B and Christiansen P J 1969 *Plasma Phys.* **11** 987
[15] Boswell R W 1984 *J. Plasma Phys.* **31** 197
[16] Sudit I D and Chen F F 1994 *Plasma Sources Sci. Technol.* **3** at press